Understanding Phonon Polaritons and Epsilon-Near-Zero Modes in Sapphire Nanocones Across the Broad Reststrahlen Band (385 cm^{-1}- 1050 cm^{-1})

Supplementary Information

Milad Nourbakhsh,[1,2] Kiernan E. Arledge,[2,3] Vincent R. Whiteside,[4] Jiangang Ma,[5] Joseph G. Tischler,[2,3] and Binbin Weng[1,2*]

[1]School of Electrical & Computer Engineering, University of Oklahoma, Norman, OK, 73019, USA
[2]Center for Quantum Research and Technology, University of Oklahoma, Norman, OK, 73019, USA
[3]Homer L. Dodge Department of Physics & Astronomy, University of Oklahoma, Norman, OK, 73019, USA
[4]Department of Electrical Engineering, University at Buffalo SUNY, Buffalo, NY, 14260, USA
[5]Center for Advanced Optoelectronic Functional Materials Research, Northeast Normal University, Changchun, Jilin 130024, China
[*]Correspondence to: Binbinweng@ou.edu

The supporting information provides additional data related to the various Reststrahlen bands of sapphire, as well as details on data acquisition, simulations, and experimental results, including Tables S1 and S2 and Figs. S1-S12.

1. Optical properties of sapphire across the broad Reststrahlen band

To better understand the Al_2O_3 crystal orientation and s and p-polarized excitations, Fig. S1 illustrates c-cut sapphire from a hexagonal crystal unit cell and various polarizations of incident light. Additionally, Fig. S2 shows the real and imaginary parts of the permittivity of sapphire over the studied spectral range of 385 -1100 cm^{-1}. As evident from the figure, the imaginary part of the out-of-plane permittivity (ε_z'') exhibits a high value at the hyperbolic type I (HT I) transition point of the material at ω= 397.52 ± 0.16 cm^{-1}, and the hyperbolic type II (HT II) transition at 582.41 ± 0.06 cm^{-1}, both occurring close to the TO phonons with A_{2u} symmetries.

Conversely, the imaginary part of the in-plane permittivity ($\varepsilon_{xx,yy}''$) exhibits a high value at the HT I transition point of the material at 439.10 ± 0.06 cm^{-1}, as well as at the HT II transition point at ω= 569.00 ± 0.04 cm^{-1}, which corresponds to the TO phonons with E_u symmetries. In our COMSOL simulations, we used the full complex dielectric function of sapphire reported by Schubert et al[1], and all simulation results were obtained by accounting for both the real and imaginary parts of the material's permittivity. The spectral ranges correspond to the material's various Reststrahlen bands (RBs) as detailed in table S1[1].

Furthermore, the experimentally measured and numerically calculated material's reflectivities at various angles of incidence from θ = 35° to θ = 65° are shown in Fig. S3. Total reflection occurs at incident angles greater than the critical angle where the condition $\varepsilon(\omega) < \varepsilon(\omega_{cut-off})$ is satisfied. Here, $\omega_{cut-off}$ represents the reflectivity cut-off frequency and defined as $\omega_{cut-off} =$

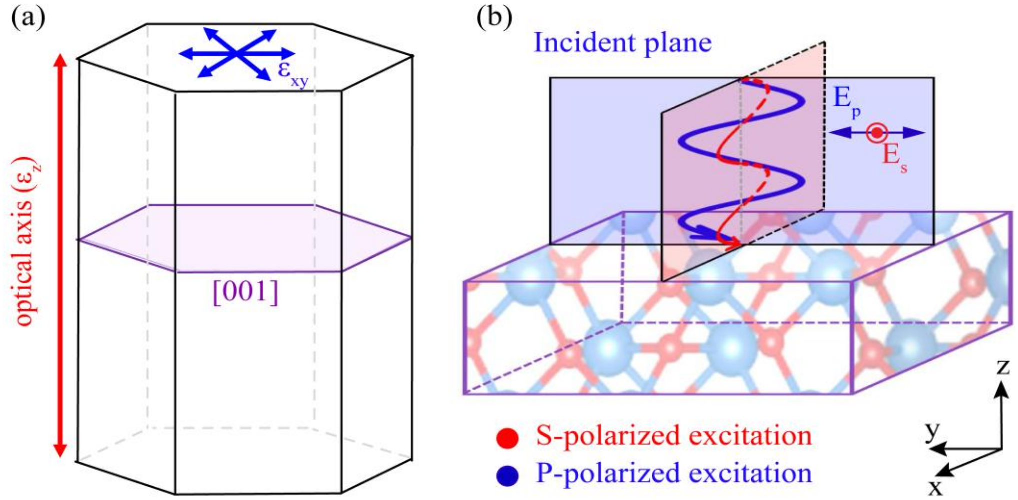

Figure S1 (a) illustrates a (001) sample cut from a hexagonal crystal unit cell, with the optic axis (c-axis) oriented perpendicular to the sample's surface. (b) Polarized components of a normal incident light beam. Here, the p-polarized light is in the YZ plane, while the s-polarized light is in the XZ plane, perpendicular to the plane of incidence.

$sin^2\theta$, where the material's reflection band drops significantly, and θ is the incident angle[1]. The cut-off frequency experiences a blueshift as the angle of incidence increases as shown in Fig. S3. For instance, the s-polarized light with incident angles of $\theta = 45°$ and $\theta = 65°$ leads to a significant drop in reflectivity at $\omega_{cut-off} \approx 962\ cm^{-1}$ and $\omega_{cut-off} \approx 1006\ cm^{-1}$, respectively. Additionally, the anisotropic feature of the material results in the p-polarized reflection band drops at lower energies than the corresponding s-polarized reflectivity ($\omega_{cut-off,z} < \omega_{cut-off,xy}$). This frequency shift occurs in the high-energy reflection bands due to the gradual variation in permittivity[1]. Furthermore, a sharp narrow band at $\omega \approx 511\ cm^{-1}$ corresponds to the LOA_{2u_1} phonon in the p-polarized excitation[1]. Here, the significant optical loss of the LO phonon inhibits near unity reflection[1]. As shown in Fig. S3, the sharpness of this peak is influenced by the angle of incidence. As the incident angle increases, the z-component of the p-polarized electric field becomes more prominent, leading to higher reflectivity. Additionally, the overlap of $A_{2u_2}$and

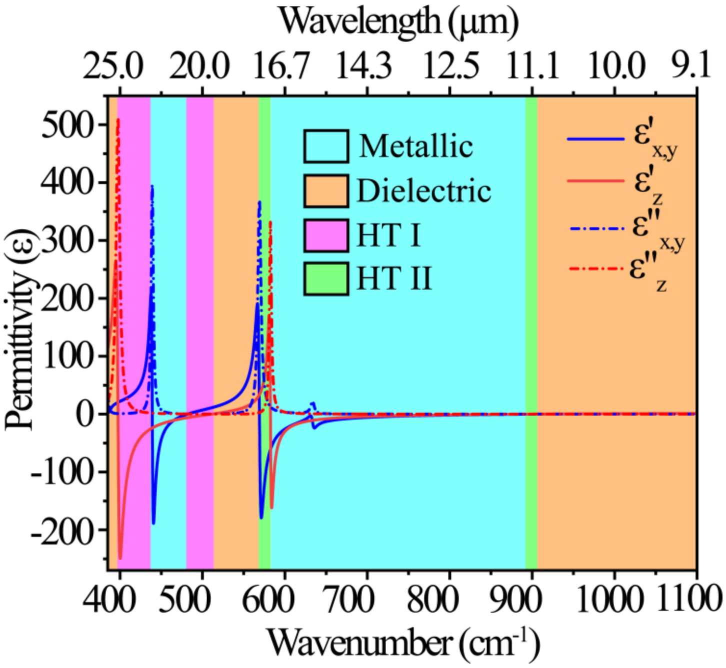

Figure S2 Real and imaginary parts of the permittivity for (001) sapphire ranging from 385 cm^{-1} to 1050 cm^{-1}. The blue curves show permittivity in x and y directions (perpendicular to the optic axis), and the red curves indicates the permittivity along z direction (parallel to the optic axis)[1]. Color coding indicates various RBs of the material which are metallic (cyan), HT I (magenta), and HT II (green).

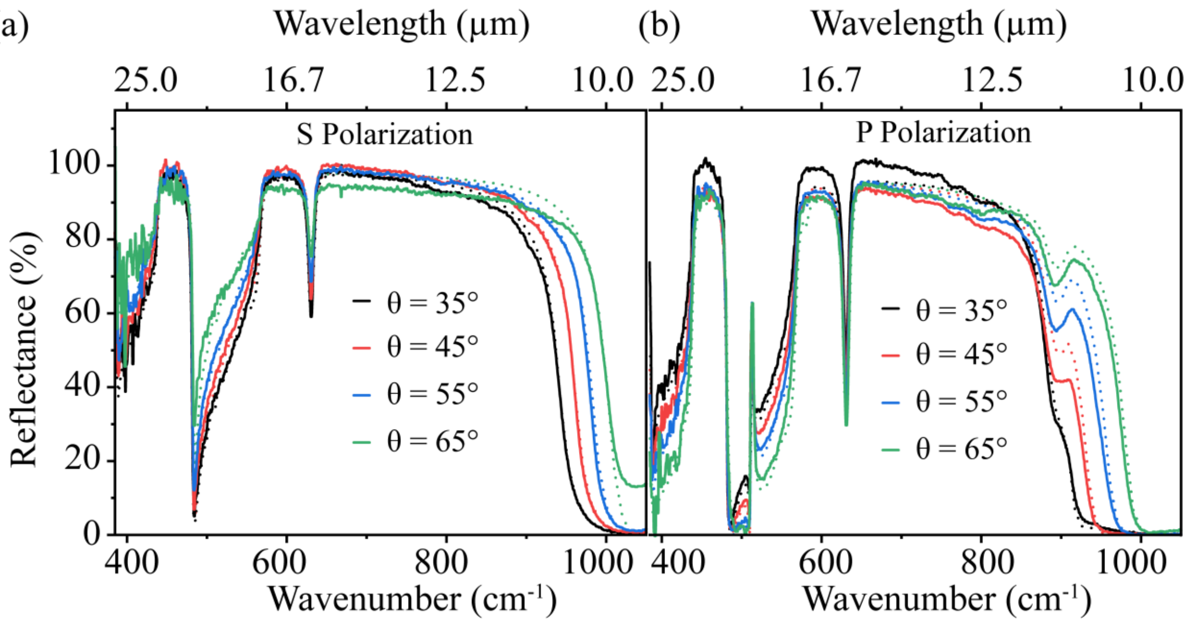

Figure S3 Experimentally measured and numerically simulated reflection spectra for bulk sapphire across a range of incident angles from θ = 35° to 65° for (a) s-polarized and (b) p-polarized excitations. For each angle of incidence, solid lines represent the experimental results, while the corresponding modeled spectra are depicted by dotted lines.

E_{u_3} bands, leads to a reflection loss at $\omega \approx 893\ cm^{-1}$ in p-polarized spectra[1].

Table S1: Spectral range in which sapphire exhibits various optical responses[1].

Optical response	Wavenumber (cm-1)	Wavelength (μm)
HT I	397.52±0.16 - 439.10±0.06	22.774±0.003 - 25.156±0.010
Metallic	439.10±0.06 - 481.68±0.05	20.761±0.002 - 22.774±0.003
HT I	481.68±0.05 - 510.87±0.02	19.574±0.001 - 20.761±0.002
Dielectric	510.87±0.02 - 569.00±0.04	17.575±0.001 - 19.574±0.001
HT II	569.00±0.04 - 582.41±0.06	17.170±0.002 - 17.575±0.001
Metallic	582.41±0.06 - 881.10±0.10	11.350±0.001 - 17.170±0.002
HT II	881.10±0.10 - 906.60±0.10	11.030±0.001 - 11.350±0.001
Dielectric	906.60±0.10 - 1050.00±0.00	9.523±0.000 - 11.030±0.001

2. Comparison of numerical modeling and experiments

A numerical analysis in the IR range was performed using finite element method in COMSOL Multiphysics. In the simulation, a periodic unit cell with infinite periodic boundary conditions was simulated, using geometric parameters derived from scanning electron microscopy (SEM) images of the nanostructure (see section 3). The unit cell was excited by a plane wave with different polarizations (Fig. S1(b)) and various incident angles.

The far-field reflection spectra for both unpatterened and structured Al_2O_3 were investigated. The numerical result for the unpatterned sapphire exhibits good agreement with the experimentally measured reflectivity data as shown in Fig. S3, thereby confirming the accuracy for the permittivity values employed in the model[1]. Additionally, a comprehensive study under various polarizations and angles of incidence reveals the presence of polariton modes for the nanocone array (NCA) structure, as shown in Fig. S4. As can be seen in the figure, the structured system mimics the behavior of the unpatterned material in the peak strength at $\omega \approx 511$ cm^{-1} and in the reflection band cut-off at high energies.

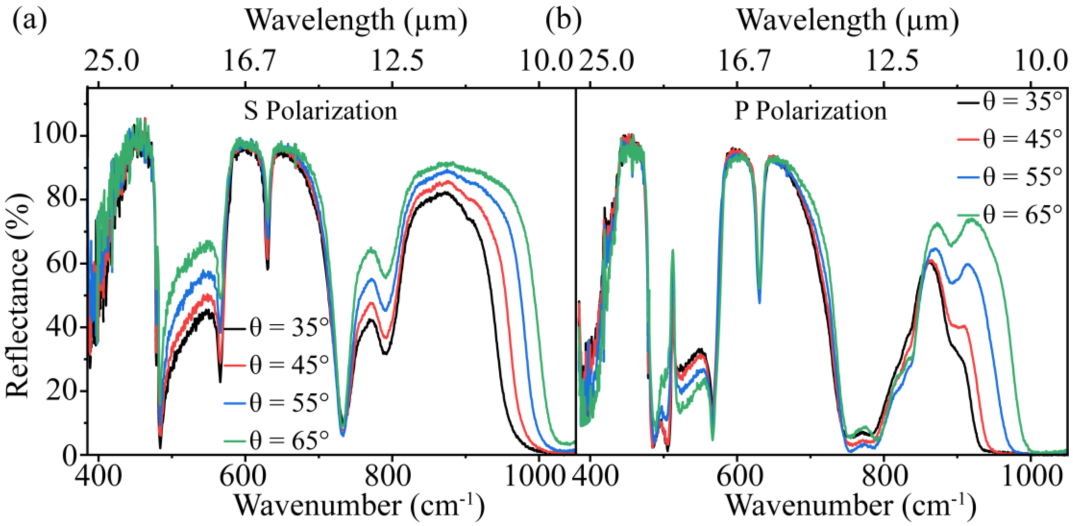

Figure S4 Experimental reflection spectra for sapphire NCA across a range of incident angles from θ = 35° to 65° for (a) s-polarized and (b) p-polarized excitations.

In an effort to uncover the impact of the shape of the NCs along on mode Ⅲ, a parallel calculation was conducted for sapphire nanocylinders with similar height ($h \approx 2\ \mu m$), period ($p \approx 3.3\ \mu m$), and diameter ($d \approx 3\ \mu m$) as the measured NCs. The results are shown in Fig. S5, where three resonances at $\omega \approx 769\ cm^{-1}$, $\omega \approx 787\ cm^{-1}$, and $\omega \approx 817\ cm^{-1}$ for the nanocylinder fall within the linewidth of mode Ⅲ. This comparison reveals that tapering the nanocylinders along the z-direction to form the NCs allows for the simultaneous excitation of multiple surface phonon

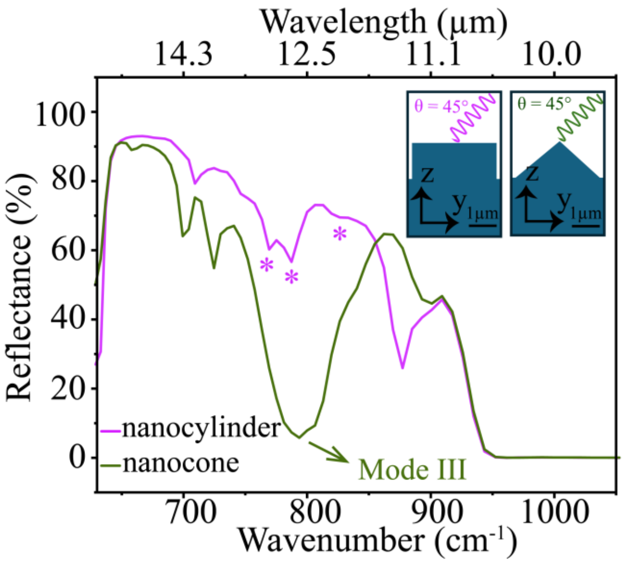

Figure S5 P-polarized calculated reflectivity corresponding to a nanocylinder structure with similar height and diameter as the NCA. The insets show a cross-sectional view of unit cell used in simulation. The 1 μm scale bars in the insets show the size of the nanostructures.

polariton (SPhP) modes at different frequencies, which overlap and result in a broader overall resonance linewidth of $148 \pm 8\ cm^{-1}$ [2,3].

Furthermore, the E-field spatial distribution corresponding to various exciting modes in the NCA system for oblique incidence of $\theta = 45°$ are shown in Fig. S6.

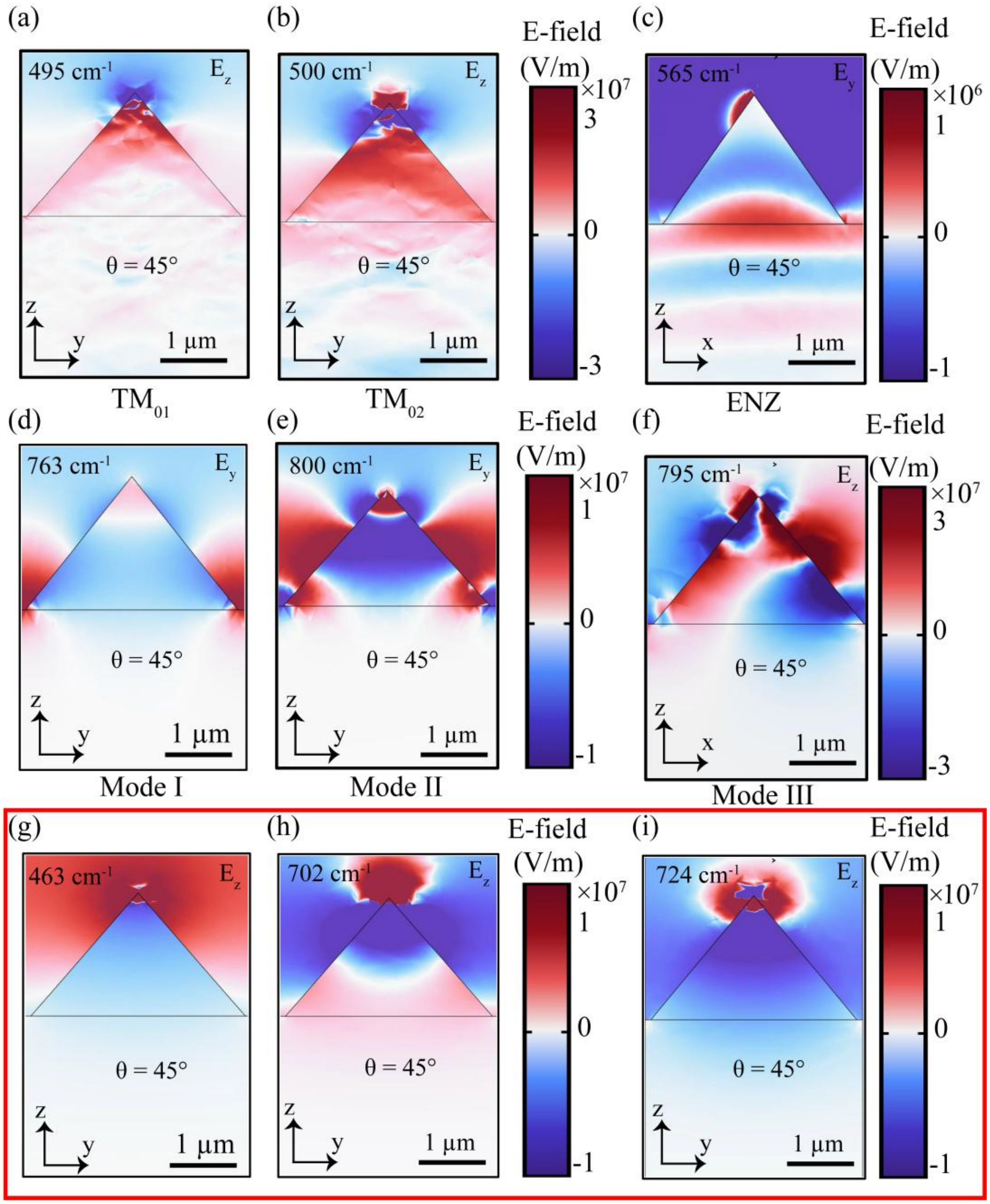

Figure S6 E-Field spatial distribution in sapphire NC for oblique incidence of $\theta = 45°$. E_z-field profiles for HVPhP at (a) 495 cm^{-1} (b) 500 cm^{-1}. E_y-field profiles for (c) ENZ mode at 565 cm^{-1} and for s-polarized SPhP resonances at (d) 763 cm^{-1} and (e) 800 cm^{-1}. E_z-field profiles for p-polarized SPhP at (f) 795 cm^{-1} and for extra observed modes in the simulation at (g) 463 cm^{-1}, (h) 702 cm^{-1}, and (i) 724 cm^{-1}. The 1 μm scale bars show the size of the NCs.

Also, to investigate the impacts of geometric parameters of the NC structure on the observed resonances, the reflection spectra of the NC structure was simulated as a function of its geometric parameters, and the results are presented in Fig. S7. The red regions correspond to a strong reduction in reflectivity, indicating the presence of SPhP modes I, II, and III. Figure S7(a) shows that the variation in NC basal diameter from 2.85 - 3.20 μm does not shift modes I and II, which is consistent with the E-field profiles shown in Figs. 3(d - e). Since modes I and II are localized at the tips and troughs of the NCs, variations in diameter do not significantly alter their modal energies. Conversely, increasing the diameter reduces the linewidth of mode III, as shown in Fig. S7(d).

Additionally, Figs S7(b) and S7(e) show that increasing the gap between NCs from 0.26 to 0.38 μm results in a redshift in mode I, while modes II and III remain unchanged. Furthermore, Figs. S7(c) and S7(f) show that the NC height is the dominant structural parameter affecting all three modes. As the height increases from 1.85 to 2.15 μm, mode I exhibits a blueshift accompanied by a reduction in intensity, whereas mode II remains spectrally unchanged but shows an increase in

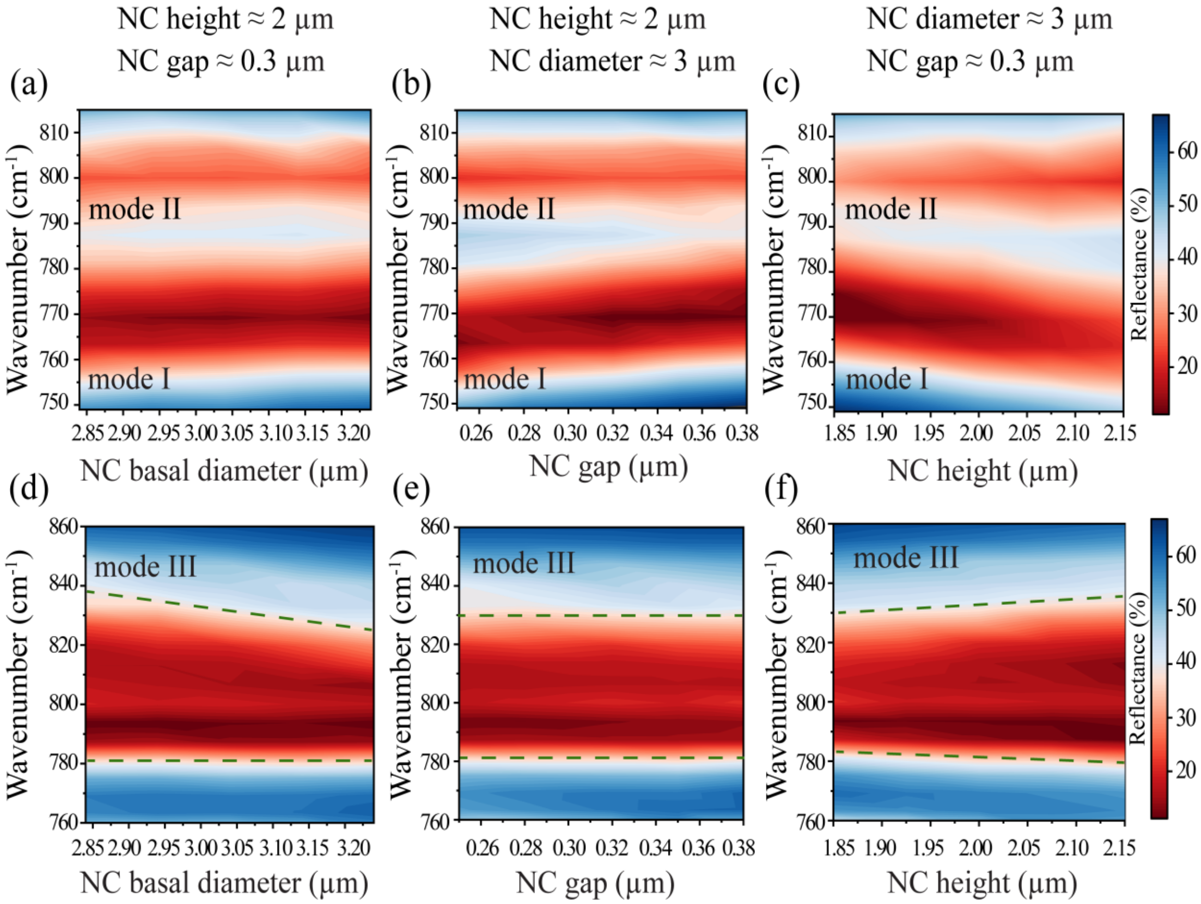

Figure S7 Effects of the NC's geometric parameters on SPhP modes in both s- and p-polarized reflection spectra with incident angle of $\theta = 45°$. Color map of the simulated s-polarized reflection spectra as a function of (a) NC 's basal diameter (b) gap between adjacent NCs (c) NC's height. Color map of the simulated p-polarized reflection spectra as a function of (d) NC's basal diameter (e) gap between adjacent NCs (f) NC's height.

intensity. Additionally, increasing the height leads to an increase in the linewidth of mode III.

In an effort to investigate the spatial phonon dispersion in sapphire NCAs, spatial Raman mappings for phonons were calculated using COMSOL Multiphysics for various cases. These cases include the coupling of A_{1g} and E_g phonons with SPhP, all hyperbolic volume phonon polaritons (HVPhPs), SPhP modes with and without the ENZ mode. To model the spatial distribution of the Raman intensity and polarizability selection rules were applied to the phonon polariton (PhP) eigenmodes of the NC structure[4,5]. The eigenmodes obtained from the reflection spectra subjected to the Raman selection rules for the A_{1g} and E_g phonon symmetries were calculated. Finally, the Raman scattering intensity was reconstructed by summing over the selected polarization intensities of PhP eigenmodes.

As shown in Fig. S8e and S8f, the phonon dispersions arise from coupling A_{1g} and E_g phonons with both optical and ENZ modes deviate significantly from the experimental data. This discrepancy arises from the fundamentally different nature of ENZ and optical phonon modes. However, as demonstrated in Figs. S8(c-d), and S8(g-h) good agreement is observed between the experimental data and the calculated spatial Raman mappings when all PhP are coupled with the phonons in NCA structure (see section 3). This shows that PhP modes couple to Raman modes while ENZ modes do not.

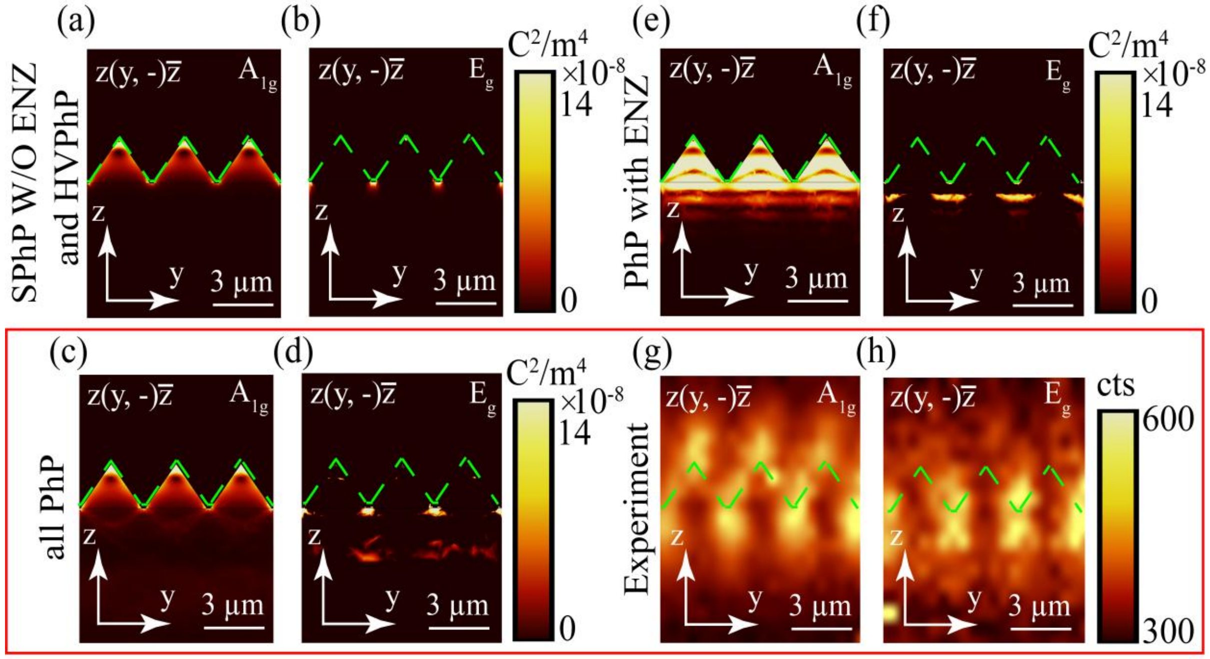

Figure S8 Comparison of simulated and measured spatial Raman mapping in ZY plane for three adjacent NCs. Calculated (a) A_{1g} and (b) E_g phonon dispersion by considering SPhP eigenmodes. Calculated (c) A_{1g} and (d) E_g phonon dispersion by considering all PhPs, including SPhPs and HVPhPs. Calculated (e) A_{1g} and (f) E_g phonon dispersion by considering PhPs and ENZ mode. Experimentally measured spatial Raman mapping for (g) A_{1g} and (h) E_g modes. The 3 μm scale bars show the size of the structure.

3. Data quantification

The data have been fitted using the Gaussian function of the form $= f_0 + A/\left(w\sqrt{\frac{\pi}{2}}\right) e^{-2\frac{(x-x_c)^2}{w^2}}$, where f_0 is a constant, A is the area, x_c is resonant frequency, and w is the width. The full width at half maximum (FWHM) is calculated as FWHM = w$\sqrt{ln4}$, and the quality factor (Q) of each mode is then calculated as Q = $x_c/FWHM$. Figure S9 shows the observed PhPs and ENZ modes along with their corresponding Gaussian fit plot. The fitting parameters for each mode are provided in Table S2.

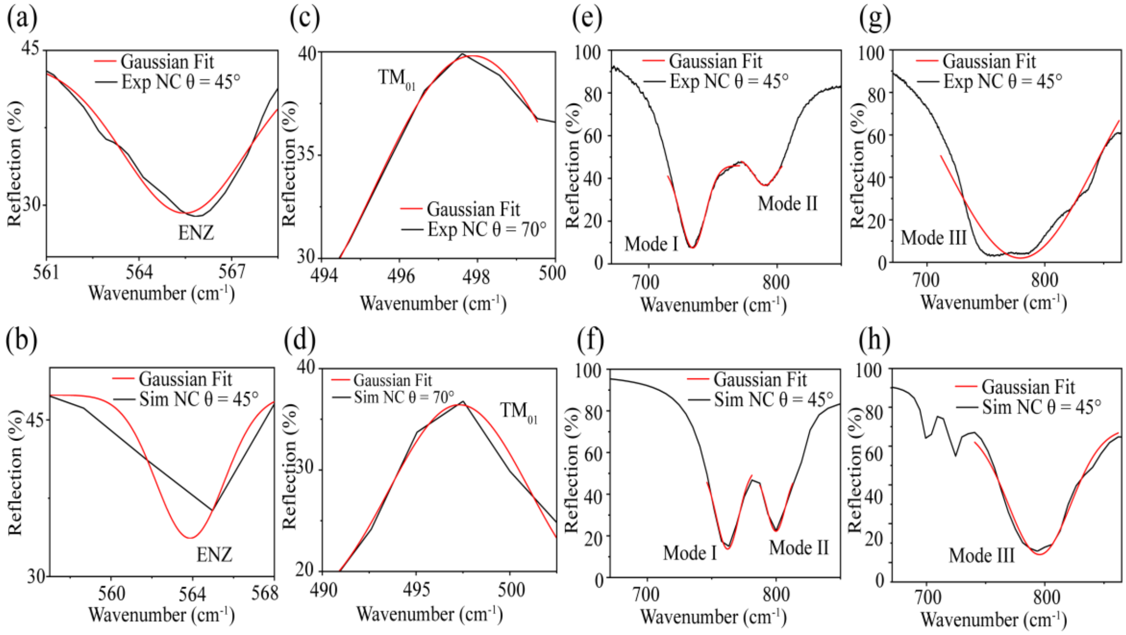

Figure S9 Gaussian fit of experimentally measured and numerically calculated reflectivity for various modes in sapphire NCA including (a-b) ENZ mode (c-d) HVPhP TM_{01} mode (e-f) s-polarized SPhP modes I and II, and (g-h) p-polarized SPhP mode III.

Table S2 Fitting parameters for the experimentally measured and numerically calculated reflectivity corresponding to each mode observed in the sapphire NCA.

Resonance	Experimental					Simulation				
	x_c	w	A	FWHM	Q	x_c	w	A	FWHM	Q
ENZ	**565.47 ± 0.05**	**3.95 ±0.27**	**-0.72 ±0.09**	**4.65 ±0.32**	**121.66 ±8.38**	**563.87 ±0.53**	**3.34 ±1.85**	**-0.57 ±0.14**	**3.93 ±2.17**	**143.48 ±79.36**
TM_{01}	**497.87± 0.04**	**5.10 ±0.22**	**1.07 ±0.08**	**6.00 ±0.26**	**82.98 ±3.60**	**497.31± 0.29**	**7.50 ±2.07**	**2.01 ±1.01**	**8.83 ±2.44**	**56.32 ±15.60**
TM_{02}	**506.86± 3.37**	**10.64 ±10.24**	**2.85 ±2.01**	**12.52 ±12.05**	**40.48 ±38.86**	**--**	**--**	**--**	**--**	**--**
Mode I	**734.32± 0.06**	**19.22 ±0.20**	**-9.27 ±0.11**	**22.63 ±0.23**	**32.45 ±0.33**	**762.32 ±0.61**	**17.38 ±3.21**	**-8.5 ±2.5**	**20.46 ±3.78**	**37.25 ±6.91**
Mode II	**790.40 ±0.05**	**16.83 ±0.31**	**-2.61 ±0.01**	**19.82 ±0.40**	**39.88 ±0.81**	**799.88 ±0.40**	**14.22 ±2.74**	**-5.00 ±1.65**	**16.74 ±3.22**	**47.7 ±9.2**
Mode III	**779.24 ±0.28**	**125.73 ±6.72**	**-173 ±22**	**148.04 ±7.91**	**5.26 ±0.28**	**795.56 ±0.76**	**52.55 ±3.5**	**-43.01 ±4.50**	**61.87 ±4.12**	**12.86 ±0.18**

For the HVPhP TM02 mode, the fractional error of 0.96 was obtained from the Gaussian fit of the experimental data. We do not report the data for the fitting of the numerical calculation of the same mode, because the error is very large and the fitting yields unreliable data.

To study the agreement between experimental results and numerical calculations, the errors for both the position and Q of each resonance were analyzed, and the results are shown in Fig. S10.

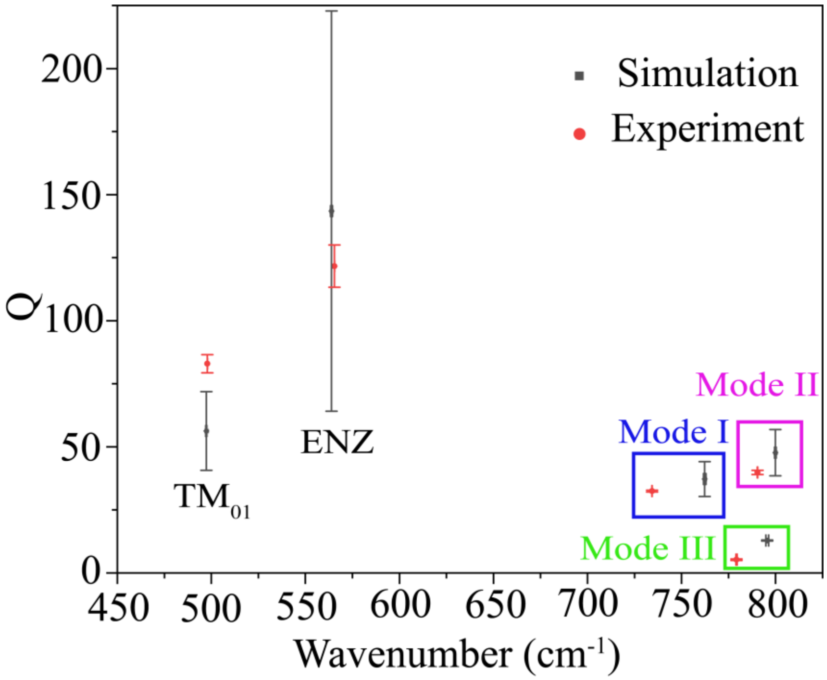

Figure S10 Error bars for the peak positions and Qs of the observed modes in sapphire NCA.

As can be seen in Fig. S10 calculations properly capture the Q factors of the ENZ mode and SPhP modes I and II showing quantitative agreement within the error bars, while providing a semiquantitative agreement for the HVPhP TM01 and SPhP III. The models also predict within error bars the energy position for the HVPhPs and ENZ modes while all the predicted SPhPs modes are blueshifted with respect to the values of the experimentally determined SPhPs. While we do not have a strong explanation for this discrepancy, we speculate that this is due to small changes in the rounding of the apex and troughs, as the HVPhPs and ENZ are volume modes. Thus, have strong dependence on the volume of the NC while the SPhPs are more dependent on the shape of the surface. The other potential explanation is that the losses (i.e., decoherence lifetime) of the higher metallic Reststrahlen band (582.41±0.06 cm^{-1} to 881.10±0.10 cm^{-1}) might be slightly higher than initially determined[1]. Adjustment of that decoherence time should shift at the SPhP modes without affecting the ENZ and HVPhP modes as the latter modes are in other Reststrahlen bands. Adjustments of the decoherence time did not account for the shift of the SPhPs. Therefore, the second explanation regarding the decoherence lifetime is somewhat less likely as the work by Schubert et al. has been very thorough.

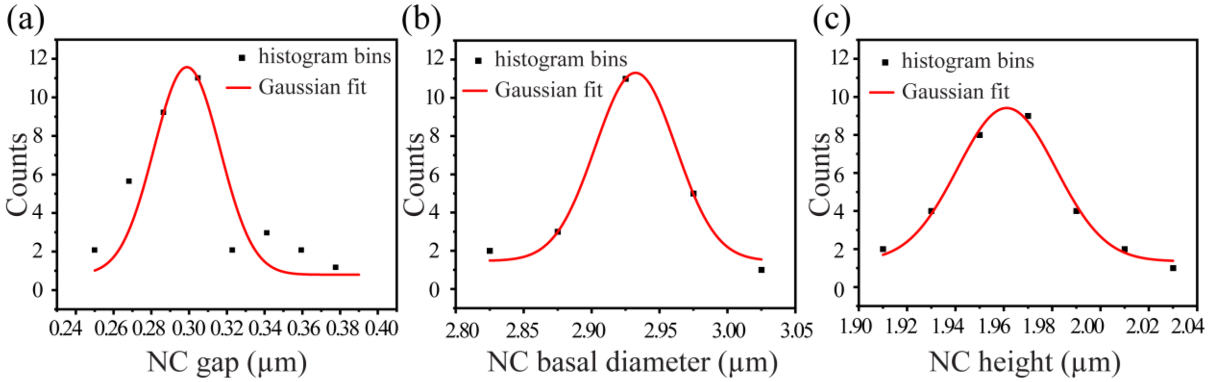

Figure S11 Central histogram bins of the repeated measurements of the NC geometries with their corresponding Gaussian fits, yielding the following measured dimensions (a) g = 0.30±0.04 μm (b) d = 2.93±0.07 μm (c) h = 1.96±0.05 μm.

To quantify the geometric parameters of the NCs, each parameter, including basal diameter (d), gap between adjacent NCs (g), and height of the NC (h), was measured 30 times through SEM images of the NCs using the image-analysis software ImageJ. Gaussian fits applied to the central bins of the corresponding histograms yielded the dimensions g =0.30±0.04 μm, d = 2.93±0.07 μm, and h = 1.96±0.05 μm, as shown in Fig. S11.

To quantify the observed enhancement in Raman signal on the nanostructure surface, the Raman spectra achieved from the bulk material and from various points on the NC were fitted using a Lorentzian function, as shown in Fig. S12. The enhancement factor was then calculated as A_{NC}/A_{Bulk} where A_{NC} and A_{Bulk} denote the integrated areas of the Raman peak for the NC and bulk material, respectively. The enhancement at the tip of the NC was determined to be 1.8 ±0.5, while the enhancement at the trough of the NC was found to be 7.0 ±0.6.

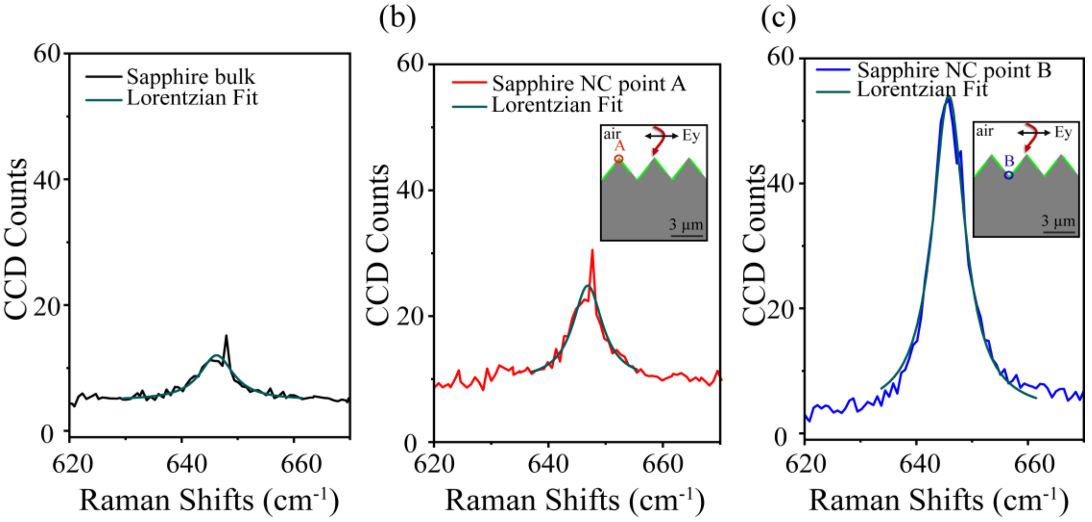

Figure S12 Raman spectra and corresponding Lorentzian fit for the Raman signal at ~645 cm^{-1} for (a) Sapphire bulk (b) at the tip of the sapphire NC, and (c) at the trough of the sapphire NC.

4. References

1 M. Schubert, T. Tiwald and C. Herzinger, *Physical Review B*, 2000, **61**, 8187.

2 Cui, K. H. Fung, J. Xu, H. Ma, Y. Jin, S. He and N. X. Fang, *Nano letters*, 2012, **12**, 1443–1447.

3 J. Yang, Z. Zhu, J. Zhang, C. Guo, W. Xu, K. Liu, X. Yuan and S. Qin, *Scientific Reports*, 2018, **8**, 3239.

4 E. Arledge, C. T. Ellis, N. R. Sarabi, V. R. Whiteside, C. S. Kim, M. Kim, D. C. Ratchford, M. A. Meeker, B. Weng and J. G. Tischler, arXiv preprint arXiv:2404.13759, 2024.

5 Bergeron, C. Gradziel, R. Leonelli and S. Francoeur, *Nature Communications*, 2023, **14**, 4098.